# Experimental Deformation of Olivine Single Crystals at Mantle Pressures and Temperatures

Paul Raterron, Elodie Amiguet, Jiuhua Chen, Li Li, Patrick Cordier

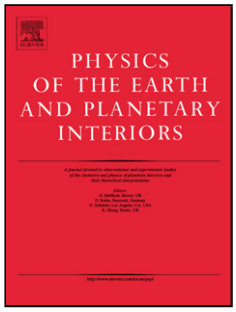


Title: Experimental Deformation of Olivine Single Crystals at Mantle Pressures and Temperatures

Authors: Paul Raterron, Elodie Amiguet, Jiuhua Chen, Li Li, Patrick Cordier

PII: S0031-9201(08)00186-6
DOI: doi:10.1016/j.pepi.2008.07.026
Reference: PEPI 5017

To appear in: *Physics of the Earth and Planetary Interiors*

Received date: 1-10-2007
Revised date: 11-7-2008
Accepted date: 21-7-2008

Please cite this article as: Raterron, P., Amiguet, E., Chen, J., Li, L., Cordier, P., Experimental Deformation of Olivine Single Crystals at Mantle Pressures and Temperatures, *Physics of the Earth and Planetary Interiors* (2007), doi:10.1016/j.pepi.2008.07.026

**REVISED VERSION 2 – R2**

# Experimental Deformation of Olivine Single Crystals at Mantle Pressures and Temperatures

Paul Raterron[1*], Elodie Amiguet [1], Jiuhua Chen[2†], Li Li[1,2], and Patrick Cordier[1]

[1]Laboratoire de Structure et Propriétés de l'Etat Solide, CNRS 8008, Université des Sciences et Technologies de Lille, F-59655 Villeneuve d'Ascq Cedex, France

[2]Mineral Physics Institute and Department of Geosciences, Stony Brook University, Stony Brook, New York 11733-2100, USA

[†] Now at: The CeSMEC, Florida International University, University Park Campus, Blg. VH150, Miami, Florida 33199, USA

* Corresponding author: Paul.Raterron@univ-lille1.fr; Tel: +33 320 43 4686; Fax: 6591

**Abstract**

Deformation experiments were carried out in a Deformation-DIA high-pressure apparatus (D-DIA) on oriented San Carlos olivine single crystals, at pressure ($P$) ranging from 3.5 to 8.5 GPa, temperature ($T$) from 1373 to 1673 K, and in poor water condition. Oxygen fugacity ($fO_2$) was maintained within the olivine stability field and contact with enstatite powder ensured an orthopyroxene activity $a_{opx} = 1$. Two compression directions were tested, promoting either [100] slip alone or [001] slip alone in (010) crystallographic plane, here called respectively a-slip and c-slip. Constant applied stress ($\sigma$) and specimen strain rates ($\dot{\varepsilon}$) were monitored *in situ* using time-resolved x-ray synchrotron diffraction and radiography, respectively. Transmission electron microscopy (TEM) investigation of run products revealed that dislocation creep was responsible for sample deformation. Comparison of the obtained high-$P$ deformation data with the data obtained at room-$P$ by Bai et al. (1991) - on identical materials deformed at comparable $T$-$\sigma$-$fO_2$-$a_{opx}$ conditions - allowed quantifying the $P$ effect on a-slip and c-slip rheological laws. A slip transition with increasing pressure, from dominant a-slip to dominant c-slip, is documented. a-slip appears sensitive to pressure, which translates into the high activation volume $V_a^* = 12 \pm 4$ cm$^3$/mol in the corresponding rheological law, while pressure has little effect on c-slip with $V_c^* = 3 \pm 4$ cm$^3$/mol. These results may explain the discrepancy between olivine low-$P$ and high-$P$ deformation data which has been debated in the literature for more than a decade.

**Keywords**: upper mantle, San Carlos olivine, high pressure, dislocation creep, slip systems, rheological law, activation volume

## 1. Introduction

Olivine deforms by dislocation creep in the shallow upper mantle, as revealed by seismic-velocity anisotropies observed in this region. Seismic velocity anisotropy is interpreted from lattice preferred orientations (LPO) produced experimentally in olivine, and allows characterization of mantle convective flows [e.g., *Montagner*, 1994; *Park and Levin*, 2002; *Debayle et al.*, 2005]. Olivine LPO depend on the dominant dislocation slip systems activated during deformation (e.g., Karato (1987), and Kaminski and Ribe (2001)). Olivine slip system relative activities have thus been extensively studied, although mostly at relatively low hydrostatic pressure ($P$ < 3 GPa) because of experimental limitations (Raleigh, 1968; Carter and Avé Lallemant, 1970; Phakey et al. 1972; Kohlstedt and Goetze, 1974; Poirier, 1975; Kohlstedt et al., 1976, 1980; Durham and Goetze, 1977; Durham et al., 1977, 1979; Gueguen, 1979; Jaoul et al., 1979; Darot and Gueguen, 1981; Gueguen and Darot, 1982; Mackwell and Kohlstedt, 1985; Ricoult and Kohlstedt, 1985; Bai et al., 1991; Bai and Kohlstedt, 1992a, 1992b; Jin et al., 1994). At $P$ < 3 GPa, mantle temperature ($T$ > 1173 K), moderate differential stress and in dry condition, olivine [100](010) and [100](001) slip systems (Pbnm space group), further referred as a-slip, dominate the less active [001](010) and [001](100) systems, here referred as c-slip. This results in deforming rocks in aligning crystal fast velocity [100] axis with the principal shear direction (e.g., Bystricky et al., 2000).

Yet, recent deformation experiments carried out at high pressure on forsterite (Fo100) crystals (Couvy et al., 2004; Raterron et al., 2007), as well as theoretical studies based on first-principle calculations (Durinck et al., 2005; Durinck et al., 2007), show that olivine c-slip may dominate deformation in the $P$ and $T$ ranges of the deep upper

mantle. This may promote a shear-parallel slow-velocity [001] axis, which could explain the seismic-velocity attenuation with depth (Mainprice et al., 2005) observed in the upper mantle. Olivine a-slip/c-slip transition has previously been attributed to the presence of water under the form of hydroxyl group in the solid solution (e.g., Jung and Karato (2001); Katayama et al. (2005); Jung et al. (2006)). A pressure effect with similar consequences would have strong implications on the geophysical interpretation of mantle seismic anisotropy, i.e., on our present understanding of mantle flows. This issue has been actively debated in the literature (Xu et al., 2007; Karato, 2007; Ji et al. 2007).

The aim of the present study was to investigate a-slip and c-slip relative activities at mantle pressure and temperature in iron bearing olivine, in order to determine if the pressure-induced slip-system transition observed in pure forsterite also occurs in natural olivine. This was achieved by carrying out deformation experiments on San Carlos olivine single crystals at mantle *P* and *T*, in a Deformation DIA apparatus (D-DIA) coupled with synchrotron radiation (Wang et al., 2003).

## 2. Samples and deformation experiments

*Sample preparation*

Ten cylindrical specimens of San Carlos olivine (Fo91) - about 1.2 mm in diameter and from 1 to 2 mm in length - were cored in a large gem-quality single crystal, and polished on both ends (with SiC paper and alumina powder, down to 1 μm). Specimens were light green, transparent and contained no detectable defect at the binocular scale. Two crystallographic orientations were chosen to promote either **a** dislocation glide or **c** dislocation glide. Specimen orientations were verified to within ± 5° by transmitted electron microscopy (TEM). Five specimens, further called a-samples, were compressed along the $[110]_c$ direction which forms a 45° angle with both

[100] and [010] crystallographic directions. This orientation promotes only a-slip in (010) plane, i.e. the [100](010) slip system with a maximum Schmid factor $S = 0.5$. The [001] direction is then perpendicular to the principal stress $\sigma_1$ which prevents any contribution of **c** dislocation glide (c-slip) to specimen deformation ($S = 0$). Five other specimens further called c-samples were deformed along the $[011]_c$ direction promoting only c-slip in (010) plane, i.e. the [001](010) slip system alone ($S = 0.5$). Although other glide planes, such as (001) for a-slip and (100) for c-slip, may be relevant for olivine deformation, the chosen geometry allows direct comparison of **a** and **c** dislocation activities without interferences from the nature of the Peierls stress in different glide planes (i.e., (001) and (100)), or from interactions between dislocations from different slip systems.

*Sample water contents*

Specimens were dry before the runs - containing less than 2 wt. ppm $H_2O$ (< 32 $H/10^6Si$) under the form of hydroxyl groups - and contained a maximum of 44 wt. ppm $H_2O$ (i.e., 700 $H/10^6Si$, sample SAN 70) after the runs (Bell et al.'s (2003) calibration), as revealed by Fourier transformed infrared (FTIR) measurements carried out on starting material and run products (see Table 1). I.R. spectra were obtained using a Thermo Nicolet 5700 spectrometer (Toulouse) or a PerkinElmer 2000 spectrometer (Lille), both fitted with a MCT/B nitrogen-cooled detector and attached to a microscope. An unpolarized beam was focused on up to 10 regions of each ~ 0.3 to 0.5-mm thick double-polished section of olivine, cut from the starting olivine crystal or the retrieved deformed specimens. Residues of the epoxy used to preserve the run products during section preparation resulted in a wide band in the middle of the spectra, which was subtracted in order to reveal the OH-bands observable in the range 3200 and 3800 $cm^{-1}$. Water contents reported in Table 1 take into account the uncertainties resulting from this operation. We use the calibration of Bell et al. (2003) to reduce the data in terms of water concentrations. Since this calibration is intended for polarized measurements,

water concentrations measured with an unpolarized beam may be underestimated by a factor of 1.5 or more (see Bell et al., 2003). We thus multiplied by 1.5 the measured water contents before reporting them in Table 1. Variations in SAN 70 and SAN 71 water contents translated into large uncertainties. We could not correlate the analysis locations within crystals (mostly the distance from crystal axis) with the hydroxyl concentration, suggesting that no proton diffusion profiles are present within samples. The heterogeneous water content in these samples may result from the presence of numerous fractures in the specimens (decompression cracks) which may have occasionally altered the FITR signal and/or possibly hosted surface hydroxyls. Unexpectedly, specimens deformed in mullite cubes (details below in the "Deformation experiments" section) contain more water than those deformed in boron-epoxy cubes usually hydrating high-pressure cells); the few water contents reported in Table 1 are, however, to scarce data to draw any conclusion on the hydration properties of high-pressure cubes.

*Orthopyroxene activity ($a_{opx}$) and oxygen fugacity ($fO_2$).*

To buffer the orthopyroxene activity ($a_{opx}$), samples were enrobed with a thin layer of enstatite powder, which was obtained by grounding down a large natural enstatite crystal free of defect at the binocular scale. Oxygen fugacity was not fully controlled during the run, although Ni-foils were used as strain markers (see below) and stayed in contact with the olivine specimens at run conditions. Ni metal was still present in the cells after the runs, and no Fe metal precipitate was detected by TEM in the bulk of the retrieved olivine crystals. This shows that specimens were maintained in between the Fe/FeO buffer and the Ni/NiO buffer $fO_2$, which at room $P$ and 1673 K corresponds to the $fO_2$ range $3\times10^{-10}$ - $3\times10^{-6}$ atm. This $fO_2$ range lays within the olivine stability field, which in nature roughly extends from the iron-wustite (IW) buffer to the quartz-fayalite-magnetite (QFM) buffer $fO_2$.

*Deformation experiments*

Specimens were deformed in between two alumina pistons, in compression along their axis, at *P* and *T* reaching respectively 8.5 GPa and 1673 K, in the D-DIA (Wang et al., 2003) that equipped the X17-B2 beam line of the National Synchrotron Light Source (upton, NY, USA). We used boron-epoxy or mullite cubic pressure media and, to compress the cells, tungsten carbide anvils opaque to the x rays and transparent cBN or sintered diamond anvils. Within the 6.15-mm D-DIA cells, alumina pistons were partly or entirely porous in order to accommodate cold compression deformation (porous-alumina cataclastic pore collapse and compaction) with as little damage as possible on specimen(s) and calibrants (Figure 1). At pressure and temperature, piston alumina is dense, hard sintered material, which ensures the continuity and resistance of the pistons.

Four of the six conducted experiments (Table 1) were carried out with two olivine crystals - one a-sample and one c-sample- placed in sequence along the compression direction and surrounded by a soft BN sleeve (Figure 1). This geometry, previously used by Raterron et al. (2007), ensures that both a-sample and c-sample (i.e., **a** and **c** dislocations) experience the same stress field during deformation. It allows direct comparison of sample deformation at run conditions, i.e., of **a** and **c** dislocation relative activities, with no need of knowing precisely the applied stress. Two other experiments (runs SAN141 and SAN142, see Table 1) were conducted at 1673 K and low stress level with only one ~ 2-mm long crystal in the cell (either a-sample or c-sample). For these latter experiments, a strong emphasize was put on applying low stress levels on the specimens (< 300 MPa), and measuring the applied stress with the greatest accuracy achievable in the D-DIA at the investigated *P*-*T*-$\sigma$ conditions (see below).

Temperature was generated using a vertical graphite furnace, and measured with two horizontal W3%Re-W25%Re thermocouples which junctions were placed next to the vertical compression column in the middle of the cell (Figure 1). We used two

thermocouples, because i) one at least was always lost during the run, and ii) we observed that furnace power-temperature relationship at given $P$ depends on furnace strain, i.e. higher power is required to achieve a given $T$ in a furnace shortened in compression than in an unstrained furnace. The uncertainty on temperature, i.e., mostly due to $T$ gradients within the cell (no pressure correction), has been previously measured in the center of similar D-DIA cell to typically less than 20 K/mm. Given the size of our specimens and calibrants and other possible sources of errors such as the effect of $P$ on thermocouple emf, we estimate run $T$ uncertainty to ±50 K.

During the experiments, specimens were first cold compressed to the desired pressure then heated to $T \geq 1373$ K. Stress free and constant $P$ and $T$ conditions were maintained in the beginning of each run until diffraction patterns arising from polycrystalline materials within the cell (olivine, spinel and alumina, see below) showed no evidence of stress remaining from cold compression, i.e., no peak broadening and similar spectra on all EDS detectors. This ensured hydrostatic condition before deformation. The inner rams of the D-DIA were then moved forward to apply stress and deformed the cell assembly at constant rates, which generally translated into specimen steady state deformation. A transition regime is often observed in the beginning of deformation, or just after changing D-DIA inner ram speed, which can translate into a changing deformation rate (observable during the experiment) and/or a changing measured applied stress (quantified after the experiment). All data reported in Table 1 correspond to constant strain rate and stress measured over typically more than 2 % sample strain, after steady state conditions were reached. During the experiments both the applied stress and resulting specimen strains, as well as $P$ and $T$, were measured in situ (see below). Specimen steady state deformation regime was therefore established independently of the mechanical status of the D-DIA, and several $P$-$T$ and $\sigma$ conditions were usually investigated during each experiment. In order to preserve specimen high-$T$ deformation microstructures, D-DIA inner rams were stopped at the

exact time of specimen quench at the end of each experiment. For the same reason, D-DIA inner-ram oil pressure was slowly decreased during decompression, while specimen length was check regularly by radiography to maintain it constant.

*In situ stress and strain measurements*

$P$, $\sigma$, and $\dot{\varepsilon}$ were monitored by time-resolved x-ray diffraction and radiography (e.g., Vaughan et al. (2000), and Li et al. (2004)). These techniques, previously used successfully (e.g., Li et al. (2006a), and (2006b); Raterron et al. (2007)), allow *in situ* measurement of the pressure and stress applied on specimens, and resulting specimen strain rates. Pressure and applied stress were measured from the quantification of x-ray peak shifts in diffraction patterns arising from stress calibrants: polycrystalline olivine and/or alumina, and/or $MgAl_2O_4$-spinel pellets placed in the compression column and separated from the sample(s) by Ni foils, and/or polycrystalline alumina pistons at sample ends (Figure 1). Except for the spinel pellets, calibrants were loose powders at the beginning of the experiment, and were sintered at pressure and temperature. Pressure was deduced from calibrant unit-cell volumes using the corresponding equations of state (for alumina and spinel: Anderson et al.(1992); see also Chang and Barsch (1973) for spinel; for San Carlos olivine: Zha et al (1998)), while stress $\sigma = \sigma_1 - \sigma_3$ was deduced from differences in the $d$ spacing characterizing lattice planes in different orientations with respect to the principal stress $\sigma_1$ (see Li et al. (2004) for details). Stress uncertainty using these techniques is fairly large, since it depends on the accuracy on the measured $d$ spacing - i.e., on the position of x-ray diffraction peak maxima and shifting toward higher energy on compression (smaller $d$ spacing) - which in turn depends on several experimental factors (see Raterron et al. (2007) for details). For this calculation, we assumed that $\sigma_1$ was homogeneous along the vertical compression column, and that the (horizontal) $\sigma_3$ was constant throughout the BN sleeve surrounding the samples. This was often verified by the consistency, within

uncertainties, in stress values measured in alumina, olivine and/or spinel pellets (Table 1).

In some cases, however, stress values obtained from different materials showed inconsistency, which then renders difficult exploiting stress data. Stress inconsistency is mostly observed at the lowest investigated temperature (1373 K, see Table 1). Although we did not fully identify the origin of this discrepancy, we list below several possible causes for it: i) at 1373 K, parts of the assembly (such as the alumina pistons) may not fully relax laterally, leading to pressure and stress gradients within the cell; ii) stress-calibrant diameter significantly depends on materials responses to cold compression - the softer, the larger diameter - which can result in sampling stress outside the compression column (i.e., lower stress than the actual applied stress). This problem mainly occurs when calibrant alignment is slightly off during data collection. Other sources of error and/or discrepancy includes: iii) different uncertainties on different equation-of-state parameters and elastic-constants used to process data from different materials; iv) stress calibrant grain growth during the run, leading to grains larger than typically 10 μm, i.e., inhomogeneous diffraction pattern with offset peak positions; v) diffraction peaks from surrounding materials (BN, metal foils, etc.) partly or totally superimposed to stress calibrant diffraction peaks, and affecting the corresponding peak positions; iv) metal strain markers partly shielding the vertical EDS detectors from diffracted x-rays.

Specimen plastic strain was measured on time-resolved x-ray radiographs collected on an x-ray fluorescent YAG crystal placed downstream with respect to the cell. These images were recorded after magnification on a CCD camera (for details, see Vaughan et al. (2000)). Sample and calibrant end positions appear as black lines on the radiographs (e.g., Raterron et al. (2007)). These lines result from x-ray absorption by 25-μm thick metal-foils (strain markers: here Ni foils). They allow measuring specimen length $l(t)$ as a function of time, from which specimen strain and strain rate can be

deduced. Specimen strain as a function of time $\varepsilon(t)$ was deduced from $l$(t) using the well known relationship: $\varepsilon(t) = \ln l_o/l(t)$ (here $\varepsilon(t) \geq 0$ in compression), where $l_o$ is the initial length of the specimen at given conditions. Steady-state strain rates ( $\dot{\varepsilon}$ ) and their uncertainties were then deduced from straight slopes observed over more than typically 1% strain on $\varepsilon(t)$ versus time plots (Figure 2), all other parameters ($P$, $T$, and $\sigma$) being constant.

**3. Specimen deformation microstructures**

Quenched run products were investigated by optical microscopy and TEM (Figure 3). Petrographic sections ~20-µm thick were prepared from the retrieved specimens. Optical investigation in between crossed Nichols often revealed undulatory extinctions. These features, also called wavy extinctions, are usually observed in olivine deformed at high-temperature by dislocation creep, and result from high density of dislocations fairly confined in sub-grain boundaries (tilt and/or twist walls). In our samples, undulatory extinctions are often visible throughout the crystals (Figure 3.a), and their maxima exhibit a marked direction which roughly corresponds to the dominant dislocation line direction (e.g., [001] in the case of edge **a** dislocations, see below).

Sections for TEM were ion thinned to electron transparency with a 5-kV argon beam, then carbon coated and investigated with a Philips CM30 electron microscope operating at 300 kV. TEM investigation revealed that a-slip (respectively c-slip) was largely dominant in the a-samples (respectively c-samples), as suggested by the high densities of the corresponding dislocations. The a-samples exhibit **a**-dislocations loops in glide configuration, i.e., confined in (010) glide plane, with long edge segments (Figure 3.b). This shows that a-dislocation glide was responsible for a-sample deformation. Numerous dislocation dipoles - in the process of annihilation (a restoration process) - were also observed in the a-samples. These dipoles are formed by two edge **a**-dislocation lines in the vicinity of each other, but in different (010) planes.

Annihilation occurred by diffusion, which left before completion little sessile loops aligned in the matrix. Many such loops are observed in the retrieved a-samples. This shows that diffusion was an active assisting process during the runs. We conclude that a-samples were deformed by climb-assisted **a**-dislocation glide, a classical deformation process at high temperature in olivine.

The c-samples exhibit numerous **c** dislocations, with long and curly edge segments at $T \geq 1473$ K (Figure 3.c). Such features are generally attributed to climb-assisted dislocation glide. In these samples, they also result from dislocation cross slip, a process that was remarkably active during deformation, as showed by numerous cross-slip evidences visible in the retrieved c-samples. Cross slip of **c** dislocations has been previously reported in olivine and forsterite crystals deformed at high-pressure and high-temperature (Li et al., 2006; Raterron et al., 2007). This process seems to characterize high-$P$ **c** dislocation motions in olivine. In our samples, it resulted in distributing dislocation screw segments among different planes (Figure 3.d), which expanded in 3 dimensions the **c** dislocation loops initially confined in glide planes. We thus conclude that **c** dislocation glide, assisted by dislocation cross slip and possibly dislocation climb, was responsible for c-sample deformation.

Finally, we did occasionally observe **c** dislocations in the a-samples and, reciprocally, **a** dislocations in the c-samples. These dislocations however often exhibit tangle and/or square-like figures characteristic of low temperature deformation [see *Raterron et al.*, 2004]. We thus interpreted them as resulting from the complex stress fields experienced by the samples during quench and decompression. We think these latter dislocations did not contributed to crystal high-temperature deformation, and are not representative of the steady-state deformation regimes investigated here.

## 4. a-sample versus c-sample plastic properties

Twenty six steady-state deformation conditions, i.e. constant measured $\sigma$ and $\dot{\varepsilon}$ at given $P$ and $T$, were achieved during the six experiments which are listed in Table 1, together with the applied $P$-$T$-$\sigma$ conditions and resulting steady-state strain rates.

*High c-slip activity at mantle P and T*

For runs SAN49, SAN52, SAN70 and SAN71, strain-rate values reported in Table 1 are informative per se, since the cell geometry ensures that both a-sample and c-sample experienced identical $P$-$T$-$\sigma$ conditions during the experiments. Direct comparison of a-sample and c-sample strain rates, thus, gives insight on which dislocation slip dominates deformation at run conditions. A striking observation on Table 1 is that, although a-sample strain rate is for 3 experimental conditions higher that c-sample strain rate (points # 3, 9, and 12), in most investigated conditions the c-sample deformed as fast, or faster, than the a-sample. Such an active c-slip cannot be attributed to the presence of water (protons) in olivine - as previously reported by several studies in the case of wet olivine samples (see Jung and Karato (2001)) - since our samples were dry during the runs (Section 2). The high c-sample strain rate, thus, indicates that c-slip is very active a process at high $P$, and that it may dominate deformation over a-slip in polycrystalline olivine at certain $P$-$T$-$\sigma$-$fO_2$ condition. This result is in good agreement with reports of a pressure-induce a-slip/c-slip transition in pure forsterite (Couvy et al., 2004; Durinck et al., 2005; Durinck et al., 2007; Raterron et al., 2007).

*Pressure effect on a-slip and c-slip activities*

In order to quantify the effect of pressure on a-slip and c-slip activities, data must be fitted to rheological laws. A general power law describing high-temperature dislocation creep in Fe-bearing olivine can be written:

$$\dot{\varepsilon} = A\sigma^n fO_2^m a_{opx}^q \exp -\frac{E^* + PV^*}{RT} \qquad (1),$$

where $A$ , $n$, $m$, $q$ are constants, $R$ is the gas constant, $E^*$ the activation energy, and $V^*$ is the activation volume which quantifies the effect of $P$ on crystal rheology. During the present experiments, $P$ and $T$ were known to within ± 50 K and ± 0.5 GPa, respectively, and $a_{opx}$ was buffered by the presence of enstatite ($a_{opx}$ =1) in contact with the samples (see Figure 3.a). The $fO_2$ was controlled to within ± 2 orders of magnitude around $3\times10^{-8}$ atm, if the effect of $P$ on solid buffer $fO_2$ is neglected (Section 2). Yet, the large uncertainty affecting $\sigma$ values - typically higher than ± 50 MPa - prevents the accurate determination of the stress exponent $n$ in Equation 1, i.e. the full determination of a-sample and c-sample rheological laws. Although combining several stress calibrants decreases $\sigma$ uncertainty as illustrated in Table 1 (points # 11, 13 and 14, see "Compatible $\sigma$ interval" column), the large uncertainties on $\sigma$ values measured at high-pressure remain a serious obstacle in reducing high-pressure deformation data in terms of rheological laws. This problem becomes even more critical at moderate temperature (typically $T$ < 1473 K), where stress gradients can remain in high-pressure cells and, in some cases, incompatible stress values are measured with different stress calibrants (e.g., Table 1, points # 7, 8, 9, and 12).

Conversely, experimental stresses are well constrained at room $P$ as well as all thermodynamical parameters leading to accurate rheological laws, as illustrated in the case of natural olivine crystals by Bai et al.'s (1991) detailed report (see also Bai et al. (1992b), and Jin et al. (1994)). Yet, extrapolation of room-$P$ rheological laws to Mantle pressure condition requires knowledge of the activation volume $V^*$ in Equation 1, which cannot be determined at a single pressure. It is therefore necessary to combine room-$P$ deformation data to high-$P$ deformation data in order to obtain complete and accurate rheological laws over a wide range of pressure. At $P$ = 0 (room $P$) Equation (1) becomes:

$$\dot{\varepsilon} = A\sigma^n fO_2^m a_{opx}^q \exp -\frac{E^*}{RT} \qquad (2).$$

Hence, high-*P* strain rates $\dot{\varepsilon}(P,T,\sigma,fO_2,a_{opx})$ can be deduced from room-*P* strain rates $\dot{\varepsilon}(T,\sigma,fO_2,a_{opx})$ by combining Equations (1) and (2):

$$\dot{\varepsilon}(P,T,\sigma,fO_2,a_{opx}) = \dot{\varepsilon}(T,\sigma,fO_2,a_{opx}) \times \exp - \frac{PV^*}{RT} \qquad (3).$$

At given *T*-σ-$fO_2$-$a_{opx}$ conditions, values of *V** can be obtained from the slopes on ln($\dot{\varepsilon}$) versus (–*P/RT*) plots, and complete rheological laws including the effect of *P* can then be written using Equation (3), by coupling high-*P* data with well established room-*P* rheological laws.

In order to obtain a-sample and c-sample complete rheological laws, we compared our data with those obtained at room pressure by Bai et al. (1991). These authors carried out creep experiments on San Carlos olivine single crystals with identical orientations than those of our samples, i.e. with $[110]_c$ and $[011]_c$ compression directions for respectively a-samples and c-samples. The *T* range Bai et al. (1991) investigated (1473 -1798 K) overlaps that of our experiments (1373 – 1673 K), and the differential stresses they applied (up to 180 MPa for c-samples) are comparable to those we applied at *T* > 1473 K (Table 1). Moreover, Bai et al.'s (1991) experiments were buffered with opx , which imposed $a_{opx} = 1$ as in our experiments, and are thus similar to our experiments with all respects but the investigated *P* range. Figures 4.a and 4.b show plots of $\log_{10}(\dot{\varepsilon})$ versus *P/RT*, respectively for a-samples and c-samples. In Figure 4, high-*P* data points are from the present study (numbers correspond the "#" column in Table 1), while room-*P* data (*P*~0) are calculated using our experimental *T*-σ-$fO_2$ values in the rheological laws proposed by Bai et al. (1991). These authors identified several mechanisms responsible for olivine dislocation creep, depending on the activated slip system(s) (i.e., the compression direction) and experimental *T*-σ-$fO_2$ conditions. They summarized their extensive data set with constitutive equations proper to each investigated compression direction, which combine contributions of two or three mechanisms operating sequentially or concurrently (see their Table 4). Since no data are available on the effect of *P* on the creep mechanisms identified by Bai et al. (1991),

we assumed for further calculation that all mechanisms related to a given slip system - i.e., either [100](010) or [001](010) in the case of a-samples or c-samples - shared the same dependence on $P$, i.e., have the same activation volumes $V^*$ in the corresponding rheological laws. This single $V^*$ translates into a single $V^*$ in the general constitutive equations including the $P$ dependence (such as Equation (3)), and can be deduced from $\ln(\dot{\varepsilon})$ versus $(-P/RT)$ plots.

We only reported in Figure 4 the data we obtained at $T$=1673 K, for which stress values are better constrained (see Table 1 and Section 2) and are comparable to $\sigma$ values reported by Bai et al. (1991). Error rectangles around high-$P$ experimental points reported in Figure 4 were calculated taking into account our experimental uncertainties on $P$, $T$, and $\dot{\varepsilon}$, as reported in Table 1. Stress uncertainties were also taken into account when calculating room-$P$ strain rates using Bai et al.'s (1991) constitutive equations: each high-$P$ point, thus, corresponds to two room-$P$ points (same symbol on Figure 4) which were plotted using either the measured minimum stress (open symbol) or the maximum stress (full symbol), as reported in the "Compatible stress interval" column in Table 1. A maximum slope and a minimum slope can thus be calculated for each high-$P$ point in Figure 4 (e.g., Figure 4.a, point # 4, and Figure 4.b, point # 10). From equivalent slopes obtained from $\ln(\dot{\varepsilon})$ versus $(-P/RT)$ plots, we deduced maximum and minimum values for $V^*$ compatible with each high-$P$ point. Finally, uncertainties on $fO_2$ were taken into account by using Bai et al.'s (1991) constitutive equations with either $fO_2 = 3\times10^{-6}$ atm to deduce maximum $V^*_{max}$ values, or $fO_2 = 3\times10^{-10}$ atm to deduce minimum $V^*_{min}$ values (strain rates increase with increasing $fO_2$). The resulting $V^*_{min}$ and $V^*_{max}$ values obtained from each high-$P$ data point, for both a-sample and c-sample orientations, are reported in Table 2. Also reported in Table 2 are $V^*$ intervals for a-sample activation volume ($V_a$*) and c-sample activation volume ($V_c$*), which are compatible with the measured $V^*$ ranges. Finally, both $V_a^*$ and $V_c^*$ mean values and corresponding uncertainties are given in Table 2. These latter values were obtained

taking into account uncertainties on average experimental values $V_i^* = (V_i^*{}_{\max} + V_i^*{}_{\min})/2$ , i.e. by applying to each of them a weight $\omega_i = 1/(\delta V_i^*)^2$ where $\delta V_i^*$ is the uncertainty $(V_i^*{}_{\max} - V_i^*{}_{\min})/2$, and using the general weighted mean value formulae:

$$V^* = \frac{\sum_i \omega_i \times V_i^*}{\sum_i \omega_i} \qquad (4).$$

The most striking observation in Figure 4 is that a-sample strain rate appears to depend strongly on pressure, while c-sample strain rate is fairly insensitive to *P*. This translates in Table 2 into the obtained high a-sample (a-slip) activation volume $V_a^* = 12 \pm 4$ cm$^3$/mol, and the low c-sample (c-slip) activation volume $V_c^* = 3 \pm 4$ cm$^3$/mol. These values are consistent within uncertainties with all data reported in Table 2 (see the "Compatible *V** interval" column). A direct implication of the measured a-slip and c-slip activation volumes is that pressure tends to inhibit a-slip activity, while it has little or no effect on c-slip activity. In other words, increasing pressure tends to promote a transition from dominant a-slip to dominant c-slip. Such a pressure-induced a-slip/c-slip transition in pure forsterite was predicted from theoretical calculation by (Durinck et al., 2005) and has been observed by (Raterron et al., 2007).

## 5. Discussion and geological implications

The present work is the first experimental evidence of a pressure-induced a-slip/c-slip transition in Fe-bearing olivine. The transition we report cannot be attributed to high water fugacity during the experiments (see Jung and Karato (2001)), since our samples were in very poor water condition all through deformation as revealed by FTIR measurements on starting materials and run products (see Section 2). It cannot be attributed to high applied stresses either (see Carter and Avé Lallemant (1971), and Jung et al., 2006), since the stresses we applied at 1673 K were relatively low (between 94

and 340 MPa), i.e. comparable to those applied on c-samples, at room *P* and in the same *T* range, by Bai et al. (1991). Let us highlight here that Bai et al.'s (1991) extensive set of data does not show any stress effect at high temperature on olivine a-slip versus c-slip relative activities, since all the rheological laws proposed by these authors exhibit the same stress exponent $n \sim 3.5$, independently of crystal orientation, i.e., of the activated slip system(s) (see also Bai and Kohlstedt (1992b), and Jin et al. (1994)). The present results, thus, confirm and extend to Fe-bearing olivine previous experimental reports (Couvy et al., 2004; Raterron et al., 2007) and theoretical studies (Durinck et al., 2005; Durinck et al., 2007) of a pressure induces a-slip/c-slip transition in pure forsterite.

*Olivine dislocation creep activation volume*

The activation volume ($V^*$) of olivine dislocation creep has been extensively debated in the literature, since a high activation volume (typically > 10 $cm^3$/mol) could promote a transition from dislocation creep to diffusion creep in the deep upper mantle (e.g., Karato and Wu (1993)). This would also impose in this region a Newtonian deformation regime (with $n = 1$, i.e., stress independent viscosity). Such a transition would not occur with typically $V^* < 5$ $cm^3$/mol. High activation volumes for olivine dislocation creep have been obtained from deformation experiments carried out at relatively low $P < 3$ GPa (e.g., 14 $cm^3$/mol in dry condition, see Karato and Jung (2003); see also Karato and Wu (1993)). Yet, low activation volumes (typically from 0 to 5 $cm^3$/mol) arise from high pressure deformation experiments (Li et al. 2006a; Raterron et al., 2007). Low activation volumes are also proposed in climb-assisted dislocation creep models deduced from high-pressure diffusion data (e.g., Béjina et al. (1999)). Bussod et al. (1993) reported an intermediate activation volume $V^*$ ranging from 5 to 10 $cm^3$/mol for polycrystalline olivine deformed at 13.5 GPa and 1873 K, but their experiments were affected by cataclastic deformation on cold compression followed by extensive dynamic recrystallization at high temperature. Most recently,

Durham et al. (this issue) also measured an intermediate $V^* \sim 9$ cm$^3$/mol for dry opx-buffered polycrystalline San Carlos olivine deformed at high-$T$ and intermediate pressure, i.e. in the $P$ range 3 - 5 GPa.

The apparent discrepancy between olivine low-$P$ and high-$P$ data may be reconciled by the present results. Indeed, the high activation volume arising from deformation experiments carried out at $P < 3$ GPa may simply result from a-slip dominant activity at low $P$ (and the corresponding high $V_a^*$), while the small activation volume obtained at high $P$ may be the result of the dominant c-slip at high pressure (and its low $V_c^*$). Figure 5 shows $\log_{10}$ of c-sample and a-sample strain rates versus $P$, for $T$=1673 K, $\sigma$ = 100 MPa, and for $fO_2$ ranging from $3\times10^{-10}$ to $3\times10^{-6}$ atm, conditions well representative of classical high-$T$ deformation experiments carried out on olivine. The modeled strain rates were calculated from *Bai et al.*'s [1991] constitutive equations (see their Table 4, *[110]c opx buffer* and *[011]c opx buffe*r equations) fitted with the proper high-$P$ term (Equation (3)), i.e., $\exp-(PV^*/RT)$ using the mean values $V_a^*$ and $V_c^*$ we obtained (Table 2) for the a-sample and c-sample, respectively. At these $T$-$\sigma$ conditions, the a-slip/c-slip transition occurs at $P \sim 7.5$ GPa in low $fO_2$ condition (dashed lines in Figure 5), while it occurs at $P \sim 8$ GPa in high $fO_2$ condition (plain lines in Figure 5). The slip-transition pressure thus appears fairly insensitive to $fO_2$, which results from the low $m$ values (see Equation (1)) reported by *Bai et al.* [1991] ($m \leq 0.36$). The transition pressure does not depend on the applied stress either since all constitutive equations proposed by these authors exhibit the same $\sigma$ dependence (i.e., $n \sim 3.5$). Figure 5 also shows that at typically $P < 4$ GPa, a-slip largely dominates deformation with an efficiency 1 order of magnitude higher than that of c-slip in terms of resulting strain rates, while conversely c-slip becomes largely dominant at typically $P > 11$ GPa. Between these two pressures, c-slip would more and more contribute to polycrystalline olivine deformation. These pressures, as well as the slip-transition pressure, depend on temperature, since Bai et al.'s (1991) constitutive equations involve different activation

energies ($E^*$ in Equation (1)). The overall effect of increasing temperature is to promote c-slip activity with respect to a-slip activity. This translates in the present model in lowering the slip-transition $P$ with increasing $T$. We calculated for instance that at $T$ = 1873 K, the a-slip-c-slip transition would occur between ~5.5 and 6.5 GPa, depending on $fO_2$ condition.

*Extrapolation to Mantle geotherms and stress conditions*

Extrapolating the model reported above for olivine single-crystal rheology to the Earth's mantle conditions is not straightforward for the following reasons: i) mantle rocks are aggregates of mostly olivine, pyroxenes, and garnet grains in different proportions, and in such multiphase aggregates the minor phases (namely pyroxenes and garnet) may influence the major phase (olivine) plastic behavior; ii) even by simplifying mantle rocks by pure polycrystalline olivine, interactions between grains and dynamic recrystallization have to be taken into account when modeling the plastic behavior of polycrystals and resulting lattice preferred orientations (e.g., Kaminski et al. (2001) and (2006)); iii) fluid fugacities, i.e. $fO_2$ and water fugacity ($fH_2O$), are not well constrained along geotherms (a review in Karato and Jung, 1998), and these parameters significantly affect olivine plastic deformation (e.g., Mackwell et al., 1985; Hirth and Kohlstedt, 1996); iv) geotherms themselves are not well constrained (within 200 K or more in the deep upper mantle), depending of the model used and/or the geodynamical context; v) finally stress levels hundreds of kilometers beneath oceans or continents are also poorly constrained, typically from 0.1 to several MPa in a context other than subduction. For all these reasons, we do not report here an exhaustive application of our findings to realistic mantle conditions. However, in order to evaluate the effect of pressure alone on mantle LPO, we used Bai et al.'s (1991) rheological laws, as modified here with high-pressure terms (Equation 3), and calculated that, at $fO_2 = 3\times10^{-8}$ atm along typical oceanic or continental geotherms (see Schubert et al. (2001)), olivine a-slip/c-slip transition would occur at $P$ ~ 6.7 GPa and $T$ ~1645 K. These $P$-$T$ conditions roughly

correspond to 200-km depth. For this calculation, we implicitly assume that mantle low stress level would not modified rheological-law stress dependence, with a stress exponent $n$=3.5 for both a-sample and c-sample rheological laws (Bai et al., 1991). With such an assumption (identical stress exponents), the slip transition depth does not depend on stress.

**6. Conclusion**

Deformation experiments were carried out on San Carlos olivine single crystals, at $T$-$fO_2$-$a_{opx}$ conditions of the upper mantle, and at stresses comparable to those applied during room-$P$ experiments. Two crystal orientations were tested in order to investigate the effect of $P$ on [100](010) and [001](010) dislocation slip systems, called here a-slip and c-slip, respectively. High-$P$ deformation data were compared with the room-$P$ data reported by Bai et al. (1991) which were previously obtained on identical materials and at similar $T$-$\sigma$-$fO_2$-$a_{opx}$ conditions. Pressure effects on both a-slip and c-slip activities were quantified (see Equation (1)), and lead to the activation volumes $V_a^* \sim 12$ cm$^3$/mol for the a-slip, and $V_c^* \sim 3$ cm$^3$/mol for the c-slip. These activation volumes translate into a pressure-induced slip transition, from dominant a-slip at low $P$ to dominant c-slip at high $P$. Our results provides an explanation for the high $V^*$ arising from low-$P$ deformation experiments, which likely results from dominant a-slip, and the low $V^*$ arising from high-$P$ experiments, likely resulting from dominant c-slip. Extrapolation of Bai et al.'s (1991) constitutive equations using the above $V$* values, to natural $P$ conditions along geotherms suggests that the a-slip/c-slip transition may occur at ~200-km depth in the Earth. We thus conclude that the slip transition reported here strongly support Mainprice et al.'s (2006) and Raterron et al.'s (2007) conclusion, i.e. that olivine pressure-induced slip transition may explain the seismic-velocity anisotropy attenuation observed in the upper mantle at depth greater than 200 km.

**References**

Anderson, O.L., Isaak, D., Oda, H., 1992, High-Temperature Elastic Constant Data on Minerals Relevant to Geophysics, Reviews of Geophysics, Vol. 30, No. 1, 57-90.

Bai, Q., Kohlstedt, D.L., 1992a, High-temperature creep of olivine single crystals. 2. Dislocation microstructures. Tectonophysics, 206, 1-29.

Bai, Q., Kohlstedt D.L., 1992b, High-temperature creep of olivine single crystals, 3, Mechanical results for unbuffered samples and creep mechanisms, Philosophical Magazine A, 66, 1149-1181.

Bai, Q., Mackwell, S.L., Kohlstedt D.L., 1991, High-temperature creep of olivine single crystals.1. Mechanical results for buffered samples, Journal of Geophysical Research, 96, 2441-2463.

Béjina, F., Jaoul, O., Liebermann, R.C., 1999, Activation volume of Si diffusion in San Carlos olivine: Implications for upper mantle rheology. *J. Geophys. Res.*, 104, 25529-25542.

Bell, D.R., Rossman, G.R., Maldener, J., Endisch, D., Rauch, F., 2003, Hydroxide in olivine: a quantitative determination of the absolute amount and calibration of the IR spectrum, Journal of Geophysical Research, 108(B2), 2105, doi:10.1029/2001JB000679, 2003.

Bistricky, M., Kunze, K., Burlini, L., Burg, J.P., 2000, High shear strain of olivine aggregates: rheological and seismic consequences, Science, 290, 1564-1567.

Bussod, G.Y., Katsura, T., Rubie, D.C., 1993, The large volume multi-anvil press as a high P-T deformation apparatus. *Pure and Applied Geophysics*, 141, 579-599.

Chang, Z.P., Barsch, G.R., 1973, Pressure dependence of single-crystal elastic constants and anharmonic properties of spinel, J. of Geophys. Res., 14, 2418-2432.

Carter, N.L., Avé Lallemant, H.G., 1970, High temperature flow of dunite and peridotite. Geological Society of America Bulletin, 81, 2182-2202.

Couvy, H., Frost, D. J., Heidelbach, F., Nyilas, K., Ungár, T., Mackwell, S. J. and Cordier, P, 2004. Shear deformation experiments of forsterite at 11 GPa - 1400°C in the multianvil apparatus. European Journal of Mineralogy, 16(6), 877-889.

Darot, M., Gueguen, Y., 1981, High-temperature creep of forsterite single crystals. Journal of Geophysical Research, 86, 6219-6234.

Debayle, E., Kennet, B. Priestley, K., 2005, Global azimuthal seismic anisotropy and the unique plate-motion deformation of Australia, Nature, 433, 509-512.

Durham, W.B., Goetze, C., 1977, Plastic flow of single crystals of olivine 1. Mechanical data, Journal of Geophysical Research, 82, 5737 - 5753.

Durham, W.B., Goetze, C., Blake, B., 1977, Plastic flow of single crystals of olivine 2. Observations and interpretations of the dislocation structures, Journal of Geophysical Research, 82, 5755 – 5770.

Durham, W.B., Froidevaux, C., Jaoul, O., 1979, Transient and steady-state creep of pure forsterite at low stress. Physics of the Earth and Planetary Interiors, 19, 263 - 274.

Durham W. B., Mei, S., Kohlstedt, D.L., Dixon, N.A., Wang L., 2008, New measurements of activation volume in olivine under anhydrous conditions, this issue.

Durinck, J., Legris, A., Cordier, P., 2005, Pressure sensitivity of olivine slip systems: first principle calculations of generalised stacking faults, Physics and Chemistry of Minerals, 32(8-9), 646-654.

Durinck, J., Carrez, P., Cordier, P., 2007, Application of the Peierls- Nabarro model to dislocations in forsterite, European Journal of Mineralogy, in press.

Gueguen, Y., 1979, High temperature olivine creep: evidence for control by edge dislocations. Geophysical Research Letters, 6, 357-360.

Gueguen, Y., Darot, M., 1982, Upper Mantle Plasticity from Laboratory experiments, Physics of the Earth and Planetary Interior, 29, 51-57.

Hirth, G., and Kohlstedt, D.L., 1996, Water in the oceanic upper mantle: implications for rheology, melt extraction and the evolution of the lithosphere, Earth Planet. Science Letters, 144, 93-108.

Jaoul, O., Michaut, M., Gueguen, Y., Ricoult, D., 1979, Decorated dislocations in forsterite. Physics and Chemistry of Minerals, 5, 15 - 19.

Ji, S., Wang, Q., Xu, Z., 2007, Reply to the comment of S. Karato on "Petrofabrics and seismic properties of garnet peridotites from the USP Sulu Terrane (China)" by Xu et al. [Tectonophysics 421 (2006) 111-127], Tectonophysics, 429, 291-296.

Jin, Z.M., Bai, Q., Kohlstedt, D.L , 1994, High-temperature creep of olivine crystals from four localities, Physics of the Earth and Planetary Interior, 82, 55-64.

Jung, H., Karato, S.I., 2001, Water-induced fabric transition in olivine, Science, 239, 1460-1463.

Jung, H., Katayama, I., Jiang, Z., Hiraga, T., Karato, S.I., 2006, Effect of water and stress on the lattice-preferred orientation of olivine, Tectonophysics, 421, 1-22.

Kaminski, E., Ribe, N.M., 2001, A kinetic model for recristallization and texture development in olivine polycrystals, Earth and Planetary Science Letters, 189, 253-2678.

Kaminski, E., Ribe, N.M., Browaeys, J.T., 2006, D-rex, a program for calculation of seismic anisotropy due to crystal lattice preferred orientation in the convective upper mantle. Geophysical Journal International, 158, 744-752.

Karato, S.I., 1987, Seismic anisotropy due to lattice preferred orientation of minerals: kinetic or dynamic. In High-pressure research in mineral physics, edited by M.H. Maghani and Y. Syono, pp. 455-471, AGU, Washington, D.C.

Karato, S.I., 2007, Comment on "Petrofabrics and seismic properties of garnet peridotites from the USP Sulu Terrane (China)" by Xu et al. [Tectonophysics 421 (2006) 111-127], Tectonophysics, 429, 287-289.

Karato, S.I., Wu, P., 1993, Rheology of the upper mantle: a synthesis, Science, 260, 771-778.

Karato, S.I., Jung, H., 1998, Water, partial melting and the origin of the seismic low velocity and high attenuation zone in the deep upper mantle, Earth Planet. Science Letters, 157, 193-207.

Karato, S.I., Jung, H., 2003, Effects of pressure on high-temperature dislocation creep in olivine, Philosophical Magazine, 83, 403-414.

Katayama, I., Karato, S.I., Brandon, M., 2005, Evidence of high water content in the deep upper mantle inferred from deformation microstructures, Geology, 7, 613-616.

Kohlstedt, D.L., Goetze, C., 1974, Low-stress high-temperature creep in olivine single crystals, Journal of Geophysical Research, 79, 2045-2051.

Kohlstedt, D.L., Goetze, C., Durham, W.B., Vander Sande, J., 1976, New technique for decorating dislocations in olivine, Science, 191, 1045-1046.

Kohlstedt, D.L., Nichols, H.P.K., Hornack, P., 1980, The effect of pressure on the rate of dislocation recovery in olivine, Journal of Geophysical Research, 85, 3122-3130.

Li, L., Weidner, D., Raterron, P., Chen, J. Vaughan, M., 2004, Stress measurements of deforming olivine at high pressure, Physics of the Earth and Planetary Interior, 143-144, 357-367.

Li, L., Weidner, D.J., Raterron, P., Chen, J., Vaughan, M.T., Shenghua, M., Durham, W.B., 2006a, Deformation of olivine at mantle pressure using D-DIA. European Journal of Mineralogy, 18, 7-19.

Li, L., Long, H., Raterron, P., Weidner, D., 2006b, Plastic flow of pyrope at mantle pressure and temperature, American Mineralogist, 91, 517-525.

Mackwell, S.J., Kohlstedt, D.L., Paterson, M.S., 1985, The role of water in the deformation of olivine single crystals. J. Geophys. Res., 90, 11,319-11,333.

Mainprice, D., Tommasi, A., Couvy, H., Cordier, P., 2005, Pressure sensitivity of olivine slip systems and seismic anisotropy of the upper mantle, Nature, 433, 731-733.

Matveev, S., O'Neill, H. ST., Ballhaus, C., Taylor, W.R., Green, D.H., 2001, Effect of silica activity on $OH^-$ IR spectra of olivine: implication for low-a$SiO_2$ mantle metasomatism, Journal of Petrology, 42, 721-729.

Montagner, J.P., 1994, Can seismology tell us anything about convection in the mantle? Review in Geophysics, 32, 115-138.

Park, J., Levin, V., 2002, Seismic anisotropy: Tracing plate dynamics in the mantle, Science, 296, 485-489.

Phakey, P., Dollinger, G., Christie, J., 1972, Transmission electron microscopy of experimentally deformed olivine crystals. In Flow and Fracture of Rocks, H. C. Heard, I. Y. Borg, N. L. Carter (Eds), C. B. Raleigh, Geophysical Monograph Series, 16, 117-138.

Poirier, J.-P., 1975, On the slip systems of olivine, J. Geophys. Res., 80, 4059-4061.

Raleigh, C.B., 1968, Mechanisms of Plastic Deformation of Olivine, Journal of Geophysical Research, 73, 5391-5406.

Raterron, P., Wu, Y., Weidner, D.J., Chen, J., 2004, Low temperature olivine rheology at high pressure. Physics of the Earth and Planetary Interior, 145 (1-4), 149-159.

Raterron, P., Chen, J., Li, L., Weidner, D., Cordier, P., 2007, Pressure-induced slip-system transition in forsterite: Single-Crystal rheological properties at mantle pressure and temperature, American Mineralogist, 92, 1436-1445.

Ricoult, D.L., Kohlstedt, D.L., 1985, Experimental Evidence for the effect of chemical environment upon the creep rate of olivine. In Schock, R.N. (ed.) Point Defects in Mineral. Geophysical Monograph Series, 31, American Geophysical Union, Washington, D.C., pp. 171-184.

Schubert, G., Turcotte, D.L., Olson, P., 2001, Mantle Convection in the Earth and Planets, Part 1, Cambridge University Press, New York, pp. 143-150.

Vaughan, M., Chen, J., Li, L., Weidner, D., Li, B., 2000, Of X-ray imaging techniques at high-pressure and temperature for strain measurements. In Manghnani, M.H., Nellis, W.J., Nicol, M.F. (eds.) AIRAPT-17. Universities Press, Hyderabad, India, pp. 1097-1098.

Wang, Y., Durham, W.B., Getting, I.C., Weidner, D.J., 2003, The deformation DIA: a new apparatus for high temperature triaxial deformation to pressure up to 15 GPa. Review of Scientific Instruments, 74, 3002-3011.

Xu, Z., Wang, Q., Ji, S., Chen, J., Zeng, L., Yang, J., Chen, F., Liang, F., Wenk, H-R. (2006) Petrofabrics and seismic properties of garnet peridotite from UHP Sulu terrane (China): Implications for olivine deformation mechanism in a cold and dry subducting continental slab, Tectonophysics, 421, 111-127.

Zha, C.-S., Duffy, T.S., Downs, R.T., Mao, H.-K., Hemley, R.J., 1998, Brillouin scattering and x-ray diffraction of San Carlos olivine: direct pressure determination to 32 GPa, Earth Planet. Science Letters, 159, 25-33.

**Acknowledgements:** The authors thank Donald Weidner (Stony Brook University, USA) for fruitful discussions, as well as Alexandre Dimanov (Laboratoire de Mécanique des Solides, France), an anonymous reviewer and William Durham (MIT, USA, this issue guest Editor) for helpful comments and suggestions to improve the original manuscript. They thank Liping Wang, Zhong Zhong and Hongbo Long (Stony Brook University, NY, USA) for their assistance at the NSLS beam line X17-B2 (supported by the U.S. Department of Energy, contract # DE-AC02_98CH10886 and COMPRES), and Jannick Ingrin (Université Paul Sabatier, France) for his assistance at the FTIR facilities in Toulouse. This research was supported by the NSF Grant EAR-9909266, EAR0135551, and EAR0229260, and the Centre National de la Recherche Scientifique CNRS / INSU Grants "DyETI 2004" and "DyETI 2005", as well as the CNRS "Programme International de Collaboration Scientifique" (PICS program). The TEM national facility in Lille is supported by the CNRS (INSU) and the Conseil Régional du Nord – Pas de Calais, France.

**Figure 1**: schematic drawing of the D-DIA cell assembly (Tc stands for "thermocouple"). The assembly height is 6.15 mm before compression. The stress calibrants used here include polycrystalline olivine, $MgAl_2O_4$ spinel and alumina (see Table 1).

**Figure 2**: a-sample (open squares) and c-sample (solid triangles) total strains versus time, for different *P*-*T*-$\sigma$ conditions, identical for both samples (see Table 1, run SAN52, points # 3 to 6). Vertical lines indicate changes in *P*, *T* and/or $\sigma$. Dashed and straight segments indicate slopes corresponding respectively to a-sample and c-sample steady-state strain rates ( $\dot{\varepsilon}$ ). Numbers next to these lines give the strain rate values (in $10^{-6}$ $s^{-1}$). Except for the first investigated *P*-*T*-$\sigma$ condition, c-sample strain rate is higher than a-sample strain rate, which results in c-sample higher total strain at the end of the run.

**Figure 3**: San70 run products, quenched from 1573 K and 8 GPa: **a)** optical micrograph in between crossed Nichols (near extinction) of the a-sample exhibiting undulatory extinctions, with maxima lining up along [001]. Note the enstatite layer surrounding the sample, which imposed $a_{opx} = 1$ during the run; **b)** weak beam dark field (WBDF) TEM micrograph (diffraction vector **g** indicated) of the a-sample showing **a** dislocations with long edge segments due to screw-segment high mobility. Also visible in the picture are numerous evidences of a restoration process in progress, i.e., dipole annihilation by dislocation climb leaving sessile dislocation loops aligned in the matrix; **c)** WBDF TEM micrograph of **c** dislocations in the c-sample exhibiting evidences of cross slip under the form of open loops (short arrows). The long dislocation edge segments result from the high mobility of screw segments; **d)** WBDF TEM micrograph showing in the c-sample details on **c** screw dislocation mobility, which is enhanced at high-*P* by extensive cross slip (short arrows).

**Figure 4**: **a)** and **b)** $\log_{10}$ of, respectively, a-sample and c-sample strain rates versus *P/RT*. The indicated maximum (plain line) and minimum (dashed line) slopes correspond to maximum and minimum values for *V** (for clarity, not all slopes are drawn). The high-*P* data points are from the present study and were all obtained at *T*=1673 K. Numbers next to these points correspond to the "#" column in Table 1. The room-*P* data (P ~0) were calculated using the corresponding $\sigma$ values (Table 1) and $fO_2$=3×10$^{-8}$ atm, with Bai et al.'s (1991) constitutive equation (see their Table 4, *[110]$_c$ opx buffer* and *[011]$_c$ opx buffer*). Error rectangles around high-*P* points were calculated taking into account uncertainties on *P*, *T*, and $\dot{\varepsilon}$ (Table 1). Stress uncertainties were taken into account when calculating room-*P* strain rates: each high-*P* point corresponds to 2 room- *P* points (same symbol) which were plotted using either the minimum stress (open symbol) or the maximum stress (full symbol), as reported in Table 1 in the "Compatible stress interval" column. The resulting maximum and minimum slopes lead to maximum and minimum *V** values for each high-*P* point. Measuring these slopes in similar ln($\dot{\varepsilon}$) versus (–*P/RT*) plots, using $fO_2$ ranging from 3×10$^{-6}$ to 3×10$^{-10}$ atm, leads to the $V^*_{min}$ and $V^*_{max}$ values reported in Table 2. See text for further explanation.

**Figure 5**: $\log_{10}$ of c-sample and a-sample strain rates versus *P*, for the indicated *T*-$\sigma$ conditions and $fO_2$ ranging from 3×10$^{-10}$ atm (dashed lines) to 3×10$^{-6}$ atm (plain lines). Strain rate values are calculated from Bai et al.'s (1991) constitutive equations (see their Table 4, *[110]$_c$ opx buffer* and *[011$_c$ opx buffer*), which we modified according to Equation (3) using the mean values reported in Table 2: $V_a^*$ = 12 cm$^3$/mol and $V_c^*$ = 3 cm$^3$/mol for the a-sample and the c-sample, respectively.

**Table 1**. Experimental conditions and results

| Run | # | *P* (GPa) | *T* (K) | $\sigma$ (MPa) | Compatible $\sigma$ interval (MPa) | a-sample strain rate ($10^{-6}$ $s^{-1}$) | c-sample strain rate ($10^{-6}$ $s^{-1}$) | Remark(s) |
|---|---|---|---|---|---|---|---|---|
| SAN 49 | 1 | 3.6 ± 0.4 | 1573 | 480 ± 120 [d] | [360, 540] | 10 ± 1 | 10 ± 1 | Boron-epoxy cube |
| | 2 | 6.2 ± 0.2 | 1473 | 1140 ± 140 [d] | [1000, 1280] | 5 ± 3 | 6 ± 4 | Final H content [a] < 80 H/$10^6$Si (< 5 wt. ppm $H_2O$) |
| SAN 52 | 3 | 8.5 ± 0.5 | 1473 | 152 ± 49 [b] | [103, 201] | 20 ± 1 | 16 ± 1 | Boron-epoxy cube |
| | 4 | 8.5 ± 0.5 | 1673 | 249 ±91 [b] | [158, 340] | 35 ± 5 | 42 ± 5 | Final blow out : samples lost |
| | 5 | 8.5 ± 0.5 | 1373 | n.d. | n.d. | 21 ± 6 | 22 ± 7 | |
| | 6 | 5.0 ± 0.3 | 1473 | 312 ± 48 [b] | [264, 360] | 33 ± 1 | 50 ± 2 | |
| SAN 70 | 7 | 8.0 ± 0.5 | 1373 | 190 ± 60 [b]<br>330 ±100 [c]<br>1260 ± 250 [d] | * | 2.0 ± 0.1 | 8.0 ± 0.5 | Mullite cube |
| | 8 | 8.0 ± 0.5 | 1573 | 700 ± 200 [c]<br>320 ± 130 [d] | * | 5.0 ± 0.6 | 10 ± 2 | Final H content [a] 700 ± 320 H/$10^6$Si (44 ± 20 wt. ppm $H_2O$) |
| SAN 71 | 9 | 6.2 ± 0.3 | 1373 | 420 ± 180 [b]<br>880 ± 170 [c]<br>1320 ± 220 [d] | * | 25 ± 3 | 14 ± 2 | Mullite cube |
| | 10 | 4.3 ± 0.2 | 1673 | 200 ± 100 [d] | [100, 300] | 12 ± 10 | 35 ± 6 | Final H content [a] 420 ± 320 H/$10^6$Si (26 ± 20 wt. ppm $H_2O$) |
| | 11 | 4.0 ± 0.5 | 1673 | 80 ± 100 [b]<br>280 ± 200 [c]<br>240 ± 110 [d] | [130, 180] | 8 ± 4 | 26 ± 7 | |
| | 12 | 3.5 ± 0.5 | 1373 | 570 ± 45 [b]<br>2150 ± 580 [c]<br>880 ± 190 [d] | * | 17 ± 4 | 15 ± 5 | |
| SAN 141 | 13 | 5.0 ± 0.5 | 1673 | 37 ± 166 [b]<br>152 ± 58 [d]<br>127 ± 55 [e] | [94, 203] | 13.6 ± 0.5 | | Boron-epoxy cube<br>2 $Al_2O_3$ calibrants<br>1 olivine cristal<br>Final H content [a] 32 ± 32 H/$10^6$Si (2 ± 2 wt. ppm $H_2O$) |
| SAN 142 | 14 | 5.8 ± 0.4 | 1673 | 140 ± 150 [b]<br>309 ± 60 [d]<br>236 ± 92 [e] | [249, 290] | | 12.0 ± 0.5 | Boron-epoxy cube<br>2 $Al_2O_3$ calibrants<br>1 olivine crystal<br>Final H content [a] < 80 H/$10^6$Si (<5 wt. ppm $H_2O$) |

Uncertainties on *P* and *T* are typically ±0.3 GPa and ±50 K. [a] *Bell et al.*'s (2003) calibration; [b] olivine stress sensor; [c] spinel stress sensor; [d] piston alumina stress sensor; [e] standard alumina stress sensor; n.d.: not determined; * incompatible $\sigma$ range. Starting material H content ~ 5 wt. ppm $H_2O$.

**Table 2:** $V^*$ values obtained for $T$=1673 K

| | Run # | $V^*_{min}$ ($cm^3$/mol) | $V^*_{max}$ ($cm^3$/mol) | Compatible $V^*$ interval ($cm^3$/mol) | Weighted mean $V^*$ ($cm^3$/mol) |
|---|---|---|---|---|---|
| a-sample | 4 | 5.3 | 14.0 | $V_a^* \in [12, 14]$ | $V_a^* = 12 \pm 4$ |
| | 10 | 7.5 | 41.3 | | |
| | 11 | 12.1 | 26.6 | | |
| | 13 | 6.9 | 21.5 | | |
| c-sample | 4 | -5.8 | 9.4 | $V_c^* \in [1, 8]$ | $V_c^* = 3 \pm 4$ |
| | 10 | -12.6 | 12.4 | | |
| | 11 | -9.1 | 7.7 | | |
| | 14 | 1.0 | 12.7 | | |

$V^*_{min}$ and $V^*_{max}$: respectively minimum and maximum $V^*$ obtained ln(Strain rate) versus $P/RT$ plots, taking into account experimental uncertainties on $P$, $T$, $\sigma$, and $fO_2$. Weighted mean $V^*$ values are obtained using Equation (4). See text for further explanation.

**Figure 1**: schematic drawing of the D-DIA cell assembly (Tc stands for "thermocouple"). The assembly height is 6.15 mm before compression. The stress calibrants used here include polycrystalline olivine, $MgAl_2O_4$ spinel and alumina (see Table 1).

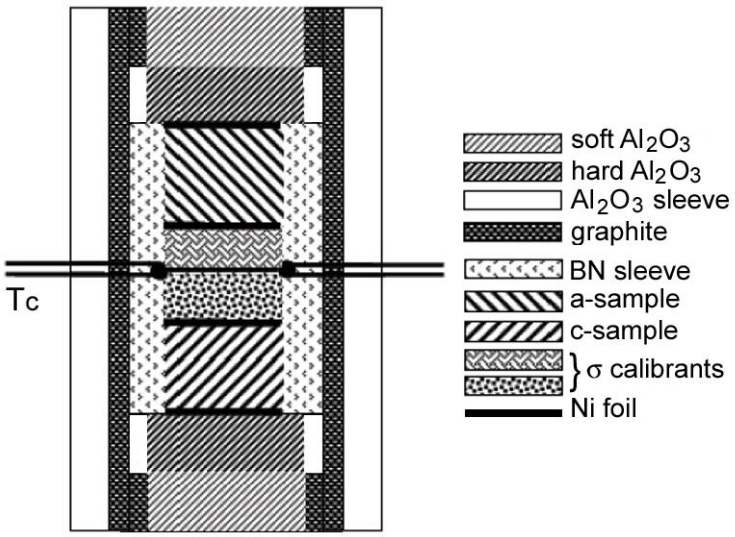

**Figure 2**: a-sample (open squares) and c-sample (solid triangles) total strains versus time, for different *P*-*T*-$\sigma$ conditions, identical for both samples (see Table 1, run SAN52, points # 3 to 6). Vertical lines indicate changes in *P*, *T* and/or $\sigma$. Dashed and straight segments indicate slopes corresponding respectively to a-sample and c-sample steady-state strain rates ( $\dot{\varepsilon}$ ). Numbers next to these lines give the strain rate values (in $10^{-6}$ $s^{-1}$). Except for the first investigated *P*-*T*-$\sigma$ condition, c-sample strain rate is higher than a-sample strain rate, which results in c-sample higher total strain at the end of the run.

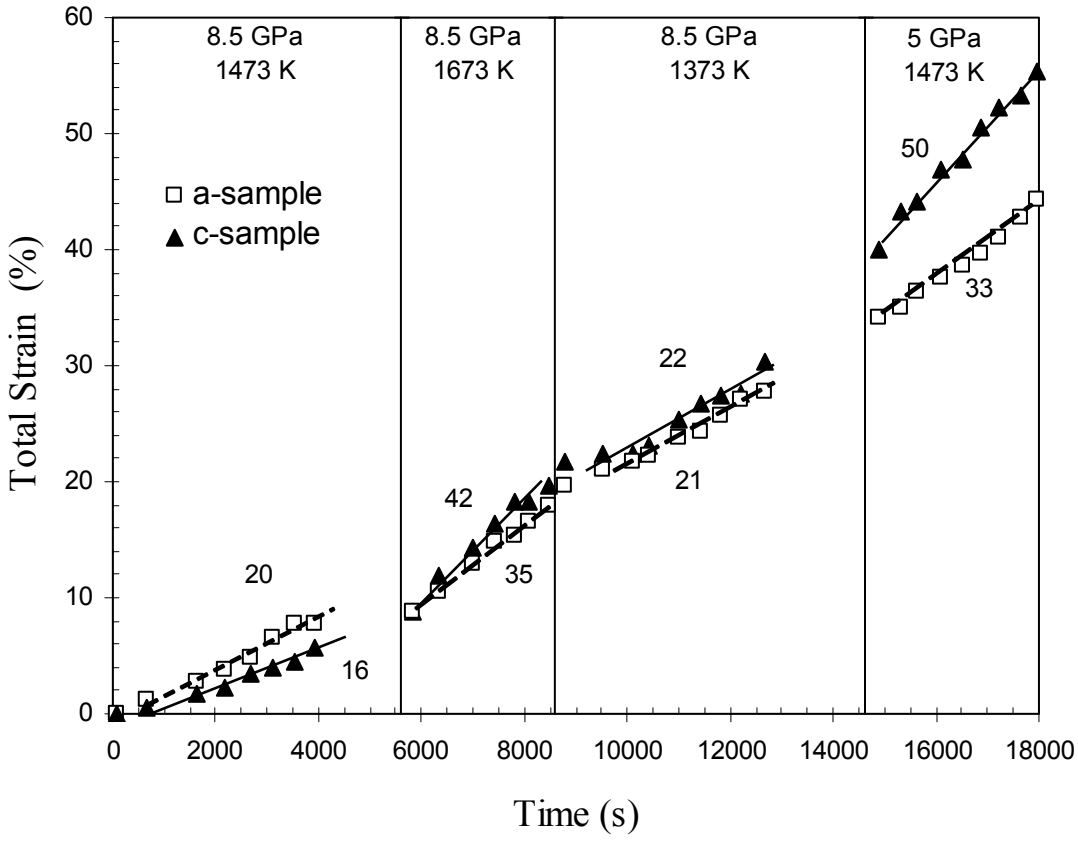

**Figure 3**: San70 run products, quenched from 1573 K and 8 GPa: **a)** optical micrograph in between crossed Nichols (near extinction) of the a-sample exhibiting undulatory extinctions, with maxima lining up along [001]. Note the enstatite layer surrounding the sample, which imposed $a_{opx}$ = 1 during the run; **b)** weak beam dark field (WBDF) TEM micrograph (diffraction vector **g** indicated) of the a-sample showing **a** dislocations with long edge segments due to screw-segment high mobility. Also visible in the picture are numerous evidences of a restoration process in progress, i.e., dipole annihilation by dislocation climb leaving sessile dislocation loops aligned in the matrix; **c)** WBDF TEM micrograph of **c** dislocations in the c-sample exhibiting evidences of cross slip under the form of open loops (short arrows). The long dislocation edge segments result from the high mobility of screw segments; **d)** WBDF TEM micrograph showing in the c-sample details on **c** screw dislocation mobility, which is enhanced at high-*P* by extensive cross slip (short arrows).

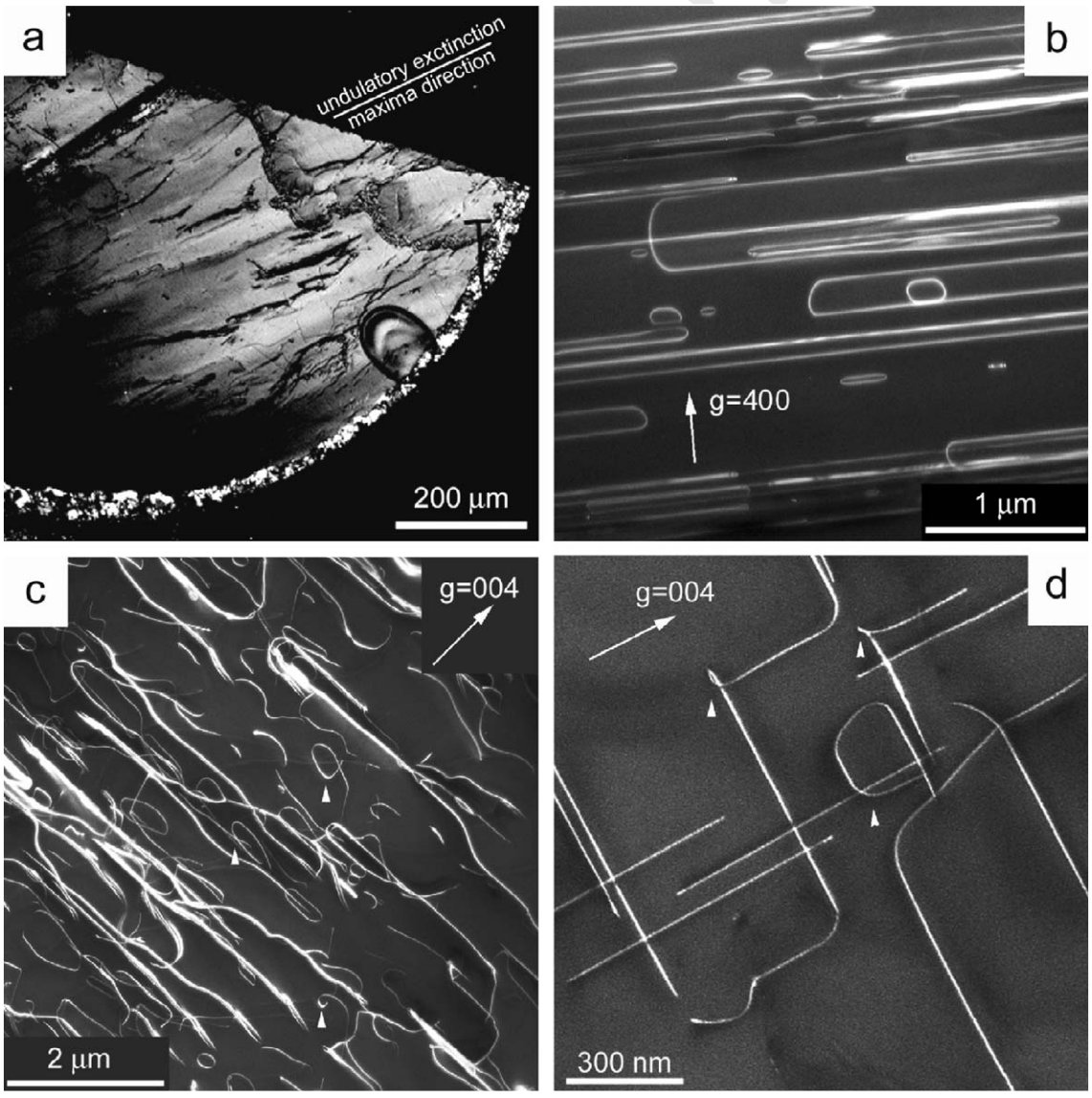

**Figure 4**: See caption page 27.

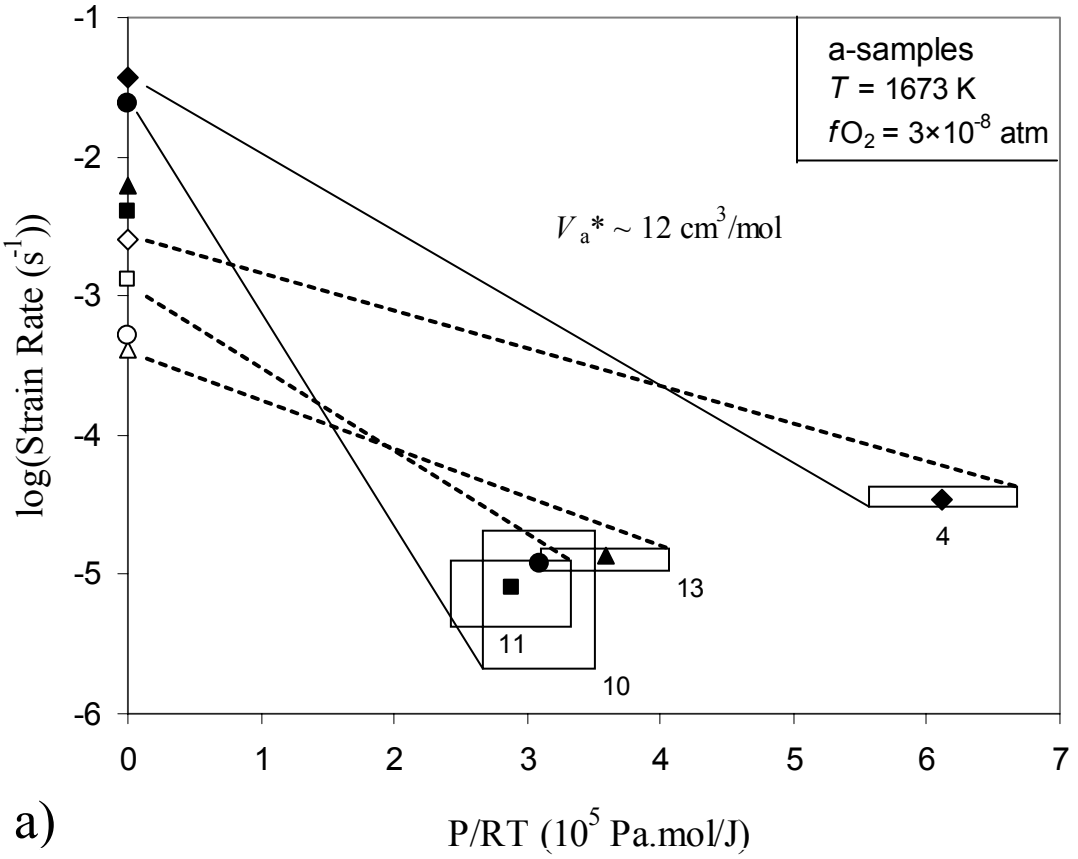


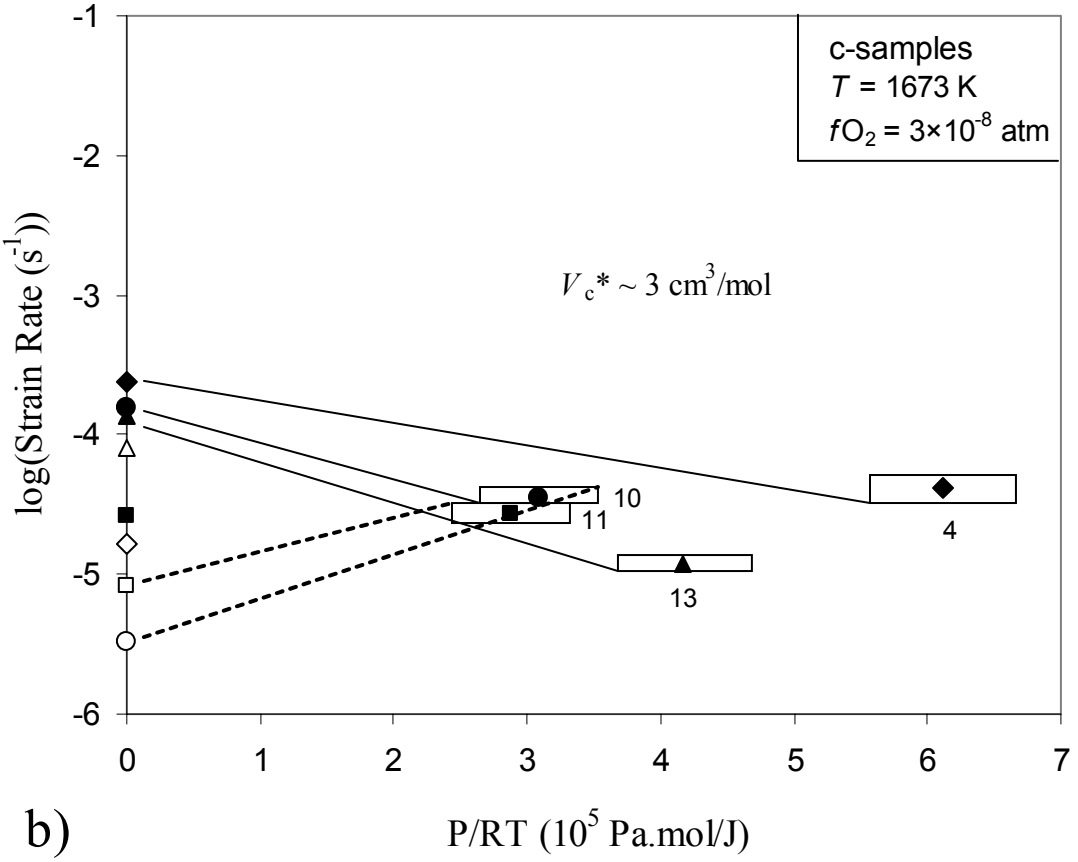

**Figure 5**: $\log_{10}$ of c-sample and a-sample strain rates versus $P$, for the indicated $T$-$\sigma$ conditions, and $fO_2 = 3\times10^{-10}$ atm (dashed lines) and $fO_2 = 3\times10^{-6}$ atm (plain lines). Strain rate values are calculated from Bai et al.'s (1991) constitutive equations (see their Table 4, *[110]$_c$ opx buffer* and *[011 $_c$ opx buffer*), which we modified according to Equation (3), using the mean values reported in Table 2: $V_a^*$ = 12 cm$^3$/mol and $V_c^*$ = 3 cm$^3$/mol for the a-sample and the c-sample, respectively.